Renewable Energy xxx (xxxx) xxx

Contents lists available at ScienceDirect

Renewable Energy

journal homepage: www.elsevier.com/locate/renene

Mean kinetic energy distribution in finite-size wind farms: A function of turbines' arrangement

G. Cortina [a, b, d, *], V. Sharma [c], R. Torres [b], M. Calaf [a]

[a] Department of Mechanical Engineering, University of Utah, Utah, USA
[b] Fluid Mechanics Department, EEBE UPC-Barcelona Tech, Barcelona, Spain
[c] School of Architecture, Civil and Environmental Engineering, EPFL, Lausanne, Switzerland
[d] Centexbel, Belgian Textile Research Centre, Technologiepark 7, 9052, Gent, Belgium

ARTICLE INFO

Article history:
Received 20 March 2018
Received in revised form
15 September 2019
Accepted 28 October 2019
Available online xxx

Keywords:
ABL-Wind farm interaction
Large-eddy simulation
Wind turbine spacing
Power-output predictor model
Wind farm efficiency

ABSTRACT

In this work the redistribution and recovery of mean kinetic energy in a realistic, finite size wind farm is studied for neutral atmospheric boundary layer conditions. Five different wind farm configurations, with different wind turbine arrangements, are considered, with four different inter-turbine spacings. By means of a localized control volume analysis, this work quantifies the mean kinetic energy recovery mechanisms as a function of downstream distance from the wind farm leading edge. Results illustrate the dependence of the mean kinetic energy distribution on the turbines' arrangement and the spatial evolution of the dominant transport mechanisms (advection and vertical flux). In the first rows of turbines, advection dominates the wake recovery, while for the last rows of turbines vertical flux of mean kinetic energy is the dominant transport mechanism. In between, a smooth transition exists between both mechanisms. From the results a low-order power output predictor model for a finite size wind farm is developed. This model allows estimating the harvested power at each wind turbine row with only the geometrical wind farm layout as an input. The low-order model is compared with other published models and validated using published experimental measurements. The new model performs very well, with errors smaller than 5%.

1. Introduction

Research regarding the optimization of wind farms' layout has been extensively developed over the past years, with the goal of designing more efficient wind energy harvesting systems. The difficulty of this problem relies on properly determining or quantifying the interaction between wind turbines and the atmospheric flow. Efforts have been focused on reducing the turbine-wake interaction to optimize wind turbine inflow conditions and thus increase the amount of harvested power per wind turbine unit [1–3]. Previous studies comprise a large amount of experimental and numerical approaches to better understand wind farm flow statistics, evaluate the potential of wind farms under different atmospheric stratifications, characterize turbine wakes, and to properly determine the utmost efficient wind farm arrangement. For example, these studies include met mast measurements, SODAR and wind LIDAR measurements taken in existing wind farms [4–8], wind tunnel experiments [9–12], as well as numerical simulations [13–18].

From these previous works, it is clear that wind farm optimization relies in the spacing between wind turbines, being one of the most important design parameters for wind farms' layouts. If a wind farm is designed with turbines too close together, there exists a reduction in harvested power because of wake-turbine interaction. Alternatively, if turbines are placed too far apart, the economical cost to implement the wind farm can increase in a substantial way.

Currently there exists a large body of literature investigating the impact of wind turbine arrangement and spacing either experimentally, or using computational tools. For example, Wu and Porté-Agel [17,18] conducted LES of staggered finite size wind farms versus aligned configurations, demonstrating that in staggered wind farms, larger separation between turbines allows wakes to recover more efficiently, hence, exposing turbines to higher local wind speeds as compared to the aligned arrangements. These

* Corresponding author. Department of Mechanical Engineering, University of Utah, Utah, USA.
E-mail address: gerard.cortina@utah.edu (G. Cortina).

https://doi.org/10.1016/j.renene.2019.10.148
0960-1481/

simulations were also in agreement with experiments from Chamorro et al. [11], which showed a higher vertical momentum transfer into the hub-height plane for a staggered wind farm than for an aligned case. Also, Stevens et al. [15] performed numerical simulations of wind farms to determine the effects of wind turbine row alignment with respect to the incoming flow direction. Various wind farms layouts with fixed streamwise spacing, and varying lateral displacements and span-wise turbine spacings, were considered. Results demonstrated that the highest power output is obtained when layouts benefit the minimization of wake-turbine interactions. Results from a perfectly aligned, semi-staggered and perfectly staggered configurations were compared, demonstrating that perfectly staggered configurations do not necessarily give the highest average power output. For example, the highest power output was found to be when an alignment angle of approximately 11° was used. In a later work, Stevens et al. [16] presented results for several wind farm configurations with different spanwise and streamwise turbine's spacing. Results showed that for wind farms arranged in a staggered configuration, the power output in the fully developed regime depends primarily on the geometric mean of the spanwise and streamwise turbine spacings. In contrast, for the aligned configuration the power output only depends on the streamwise turbine spacing. This was also previously reported by Yang et al. [14], where it was demonstrated that for aligned very large wind farms, the power production is highly dependent on the turbine's streamwise spacing, with a diminished dependency on the spanwise spacing.

In companionship to this research, there has also been important efforts in developing simplified analytical models that help predict wind farm power output without need of expensive numerical simulations. Good examples are the Jensen and the Katic-Park [19,20]; or even more sophisticated models [2,21], to characterize wind turbine wakes and potentially estimate the spread of the velocity deficit downstream of the wind turbines. All these works had the unique goal of optimizing or maximizing the amount of power that can be harvested from the atmospheric flow. For example, a recent study [22], that follows a previous work of Meyers and Meneveau [13], combines economic and fluid dynamic models to determine the most optimal spacing in very large wind farms. Results demonstrated optimal turbine spacings of the order of 10 turbine diameters or higher, even showing that 15 turbine diameters can be an optimal spacing under some reference dimensionless cost parameters. Another approach is the one illustrated in Bokharaie et al. [23]. In this case, the authors used a hybrid between the Jensen model and LES to optimize the wind turbine power extraction under neutral atmospheric stability conditions. Interestingly, given a wind-farm with known dimensions and a number of wind turbines, the optimized location of the wind turbines is highly dependent on the local wind rose. For example, it was found that for a wind farm with a dominant wind direction, turbines clustered together at the front and the back of the wind-farm would allow for maximum wake recovery in between rows and hence would be the most optimal. On the other hand, for wind farms with a uniformly distributed wind rose, best would be to have turbines evenly spread over the wind farm area.

The present work follows a previous study of Sharma et al. [24], where LES of finite size wind farms were performed to compute three different variables: the wind-farm induced effective surface roughness, the wake viscosity, and the wake-expansion coefficient. In that study, the goal was to improve parametrizations of current wind farms and wake-models. Alternatively, in this work we strive to create new knowledge on the wake recovery process in finite size wind farms as a function of the layout, under neutral stratification conditions. Works of Cortina et al. [25] and Allaerts and Meyers [26] have demonstrated that there exists two mean kinetic energy (MKE) based wake recovery mechanisms that primarily contribute to the wakes' recovery. These are the advection and the vertical flux of mean kinetic energy. Results from Cortina et al. [27] in a very large wind farm further illustrated that these mechanisms are modulated by the background thermal stratification, as well as the wind farm density. For low-dense wind farms advection dominated the wake recovery, while for high-dense wind farms the MKE recovered through fluxes of MKE. For the cases in between, a smooth balance of both mechanisms existed. In the present work the effect of the wind farm finite size is further taken into consideration. Because of the high cost of the numerical simulations developed in this study, and as a first step in this direction, this work focuses on studying the flow through a finite size wind farm under neutral stratification. The additional effects induced by thermal stratification, while important, are left for a later work.

In summary, the objective of this research is to study the evolution of the MKE terms as a function of downstream distance within finite size wind farms, taking into account the influence of the wind farm layout. Details can be found in Section 2, where the numerical simulations are described and the distinct study cases are listed. In Section 3 the main wind farm flow field statistics are presented. In Section 4 the MKE analysis is presented and results are interpreted in Section 5. On a second stage, results are further used to develop a low-order power output predictor model to estimate wind farms' power output as a function of their geometric layout (see Section 6). Results from the model are further validated in Section 7. Comparison is made with previous experimental measurements from the Horns Rev and Nysted wind farms [8,28,29], and data-sets from other published models [21], and LES data-sets [15] independent from this analysis. Finally, in Section 8 conclusions are stated, providing closure to the overall work.

2. Large Eddy simulation & study cases

The LES code used in this work solves the equations of conservation of mass (continuity) together with the momentum equation for an incompressible flow (Navier-Stokes). As is intrinsic to the LES methodology, only the large, energy-containing eddies are resolved, and the smaller ones are parametrized using a subgrid-scale model, in this case the constant Smagorinsky model [30]. The flow is forced with a constant pressure gradient in the streamwise direction. The surface roughness length is imposed to be equal to $z_0 = 0.1$ m, representative of a cultivated area with regular cover of low crops. The streamwise and spanwise numerical discretization is based on pseudo-spectral methods, with Fourier transform based differentiation. For the vertical direction, a second-order finite-differences scheme is used. The time integration is performed using the second-order Adams-Bashforth scheme. Regarding the boundary conditions, at the top of the domain a stress free condition is imposed. At the bottom surface a no-slip condition is imposed for the vertical velocity and a shear stress for the horizontal momentum components using the log-law. Because of the spectral approach in the horizontal directions, the flow is in principle periodic between the inlet and outlet regions, as well as in the lateral directions. For this purpose, to model a finite size wind farm a very large numerical domain is needed, such that it provides enough physical space for the flow to fully recover ahead and after the wind farm. For further details please refer to the Appendix section.

The domain size is set equal to $(32\pi \times \pi \times 1)$ km, in the streamwise, L_x, spanwise, L_y, and vertical directions, L_z, respectively. The

Please cite this article as: G. Cortina et al., Mean kinetic energy distribution in finite-size wind farms: A function of turbines' arrangement, Renewable Energy, https://doi.org/10.1016/j.renene.2019.10.148

boundary-layer height is set equal to the domain vertical size ($L_z = z_i = 10D$), where D represents the wind turbine rotor diameter set equal to 100 m, and z_i represents the boundary layer height. Moreover, to properly reproduce the effect of the wind turbines, and at the same time capture the mid- and far-wake regions, the domain is discretized with a numerical grid with $4096 \times 128 \times 128$ grid-points, resulting in a numerical resolution of $24.5 \times 24.5 \times 7.85$ m, correspondingly (see Fig. 1 for more details about the configuration of the LES domain). Notice that the flow is aligned with the finite-size direction of the wind farm, hence the infinite lateral size of the farm excludes the study of the lateral wind farm effects. The effect of the wind turbines is included by means of a drag-force term on the right hand-side of the Navier-Stokes equations. The drag-force parametrization utilized is the actuator-disk with rotation approach of [31], and [32]. The derivation begins using the blade element-momentum (BEM) theory which combines the concept of conservation of linear and angular momentum with the blade element forces based on the premise that these forces are solely responsible for changes in momentum of air passing through an annular disc. It is assumed that the blades are 'optimally adapted' to the time-averaged incoming velocity (V) such that the tip-speed ratio ($\lambda = \omega R/V$) remains constant. It is also assumed that the ratio of lift and drag coefficients of the blade are kept constant using active pitch control. Balancing the lift and drag forces with the change in momentum and recasting the resulting equations in standard expressions for thrust and drag forces results in new coefficients C'_P and C'_T which are related to standard coefficients as $C'_P = C_P/(1-a)^3$ and $C'_T = C_T/(1-a)^2$ respectively. In this work, values for C'_P, C'_T and a are chosen as 0.8, 1.334 and 0.25, respectively. The angular velocity (ω) is fixed at 1.5 rad/s. These values are similar to the values used in Ref. [31].

For the numerical simulations, a set of five different wind farm configurations have been considered. The same study cases have also previously been considered in Sharma et al. [24]. The study cases have been purposely configured to study the effect in the MKE redistribution for different streamwise and spanwise turbine's spacing. Table 1 outlines the different study cases. The *'baseline'* case (AL-1) consists of a wind farm composed of 24 rows of 8 turbines each (see second column of Table 1). In this case, a traditional spacing of $s_x = 7.5D$ and $s_y \approx 4D$ is considered. Three aligned cases considering different spacings have additionally been considered. These represent the combinations of changing the streamwise and spanwise turbines' spacing. The ST case, which conforms a staggered case, is used to evaluate the influence of an aligned wind farm versus a staggered one. Note that all wind farms have the same streamwise length ($L_{wf} = 18$ km), hence those wind farm configurations with $2s_x$ spacing between turbines are only composed of 12 rows of turbines, instead of 24. Finally, it should be noticed that the wind farm is finite in the streamwise direction, and occupies only 17.9% of the streamwise length of the computational domain.

Table 1
Summary of the different LES study cases for the different wind farm configurations. The first column lists the different study cases, where AL refers to aligned wind farms and ST refers to a staggered layout. The geometric mean turbine spacing is denoted by s, where $s = \sqrt{s_x s_y}$ with s_x denoting the streamwise and s_y denoting the spanwise spacing between turbines.

Study case	No. of turbines	Spacing	$s = \sqrt{s_x s_y}$
AL-1	192 (8 × 24)	s_x, s_y	5.55D
AL-2	96 (4 × 24)	s_x, $2s_y$	7.85D
AL-3	96 (8 × 12)	$2s_x$, s_y	7.85D
AL-4	48 (4 × 12)	$2s_x$, $2s_y$	11.10D
ST	192 (8 × 24)	s_x, s_y	5.55D

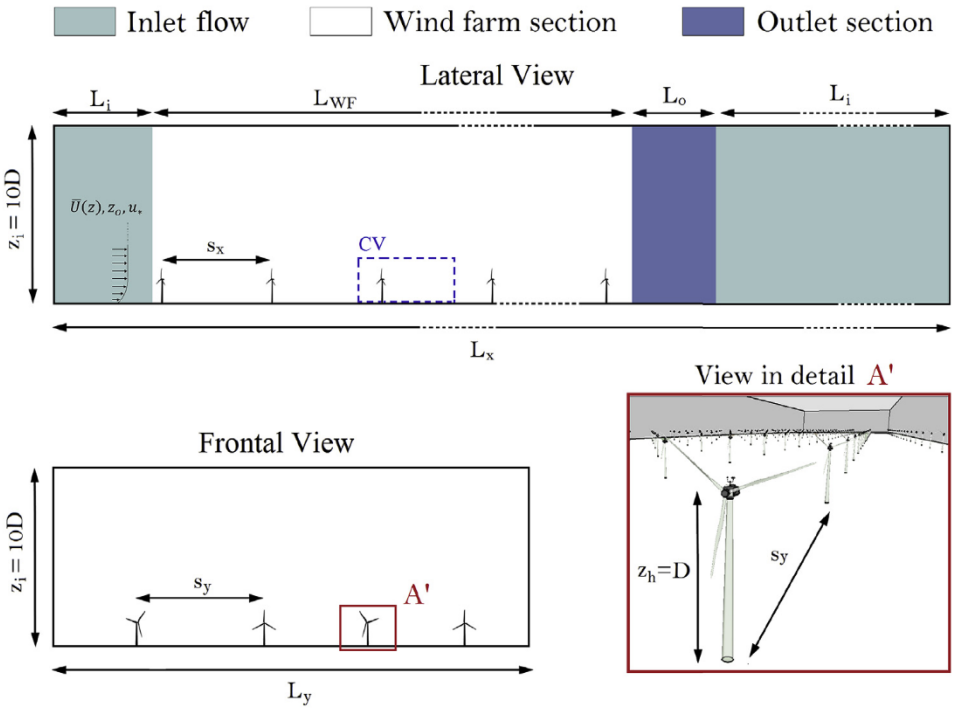

Fig. 1. Schematic representation of the baseline wind farm configuration. Top figure: lateral view of the LES domain in the streamwise direction. Bottom left: frontal view of the wind farm. Bottom right: detailed view of the highlighted A′ region in the bottom left sub-figure. In the top-figure, the blue dashed-line illustrates the control volume that will be used later in Section 4 to compute the MKE budget as a function of wind farm row. (For interpretation of the references to colour in this figure legend, the reader is referred to the Web version of this article.)

Please cite this article as: G. Cortina et al., Mean kinetic energy distribution in finite-size wind farms: A function of turbines' arrangement, Renewable Energy, https://doi.org/10.1016/j.renene.2019.10.148

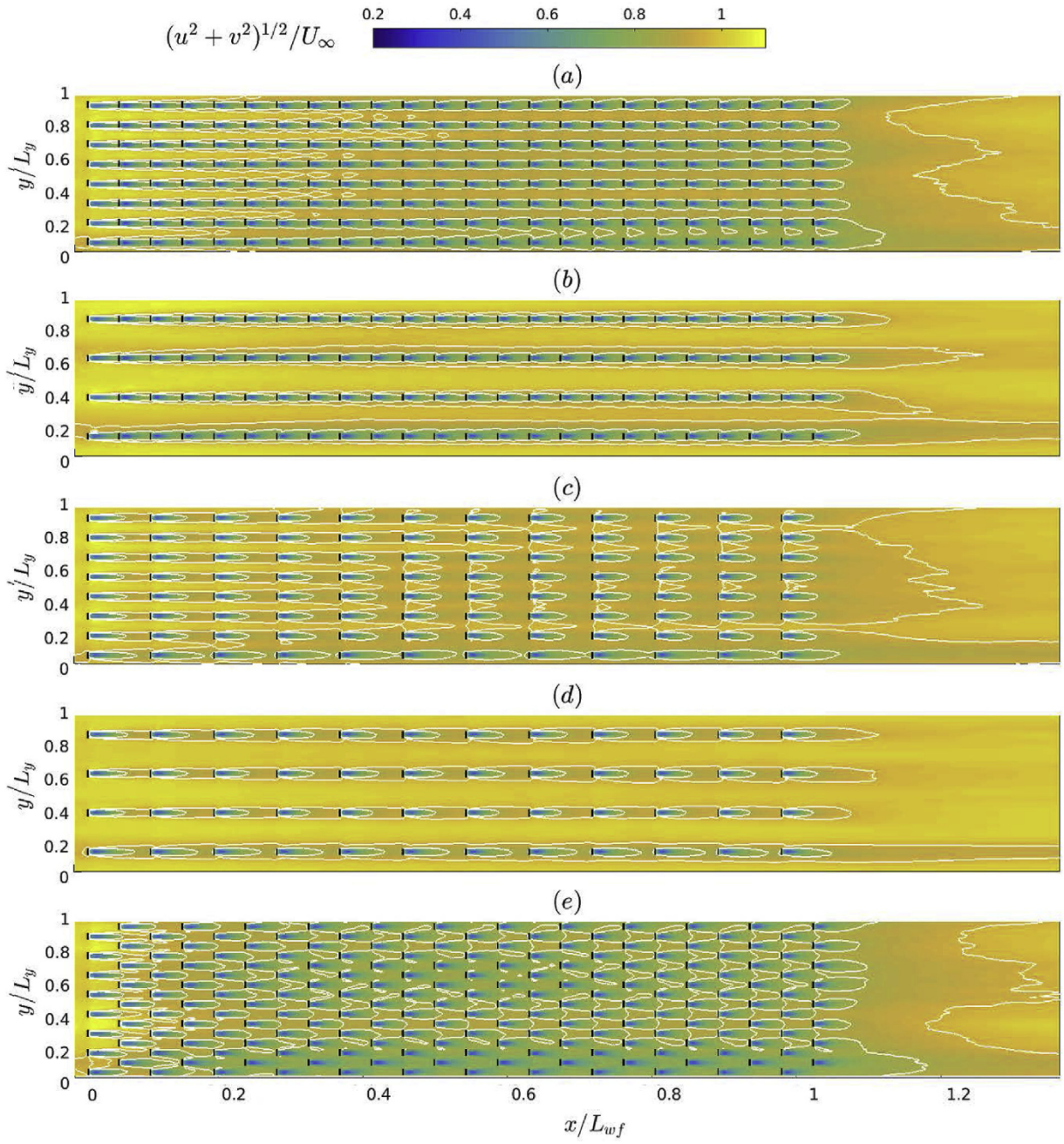

Fig. 2. Time averaged wind velocity normalized by the unperturbed inflow wind at the turbines hub-height for the different study cases, (a) AL-1, (b) AL-2, (c) AL-3, (d) AL-4, and (e) ST case. The x-axis is normalized by the streamwise wind farm length, $L_{wf} = 18$ km, and the y-axis is normalized by the spanwise wind farm length, L_y. The black lines denote the location of the wind turbine rotor disk, and the white lines depict the 85% and 95% iso-countours of velocity magnitude. Note that the figure represents only 25% of the full numerical domain.

3. Wind farm flow field statistics

Before discussing the results for the MKE budget analysis, Figs. 2 and 3 illustrate the time average normalized wind velocity and vertical shear stress, respectively. All five cases are integrated for a million time-steps representing $T_* = T\,u_*/z_i = 450$ non-dimensional time-units and an additional 200,000 steps are used to calculate statistics (which corresponds to $T_* = 27$). Both figures provide a clear representation of the main flow statistics representative of the different study cases, illustrating important features of the flow characteristics of each wind farm layout. Understanding of these flow characteristics will aid on the posterior interpretation of the MKE budgets for the different study cases. It should be mentioned that both figures strive to proportionate a visual and qualitative understanding of the different configurations of wind farms, and to detect, before entering in detail into the MKE analysis, important features of the flow. For more specific details on the flow characteristics see Sharma et al. [24].

Regarding the velocity magnitude of case AL-1 (see Fig. 2a), it is interesting to note the evolution of the turbines' wakes and their

Please cite this article as: G. Cortina et al., Mean kinetic energy distribution in finite-size wind farms: A function of turbines' arrangement, Renewable Energy, https://doi.org/10.1016/j.renene.2019.10.148

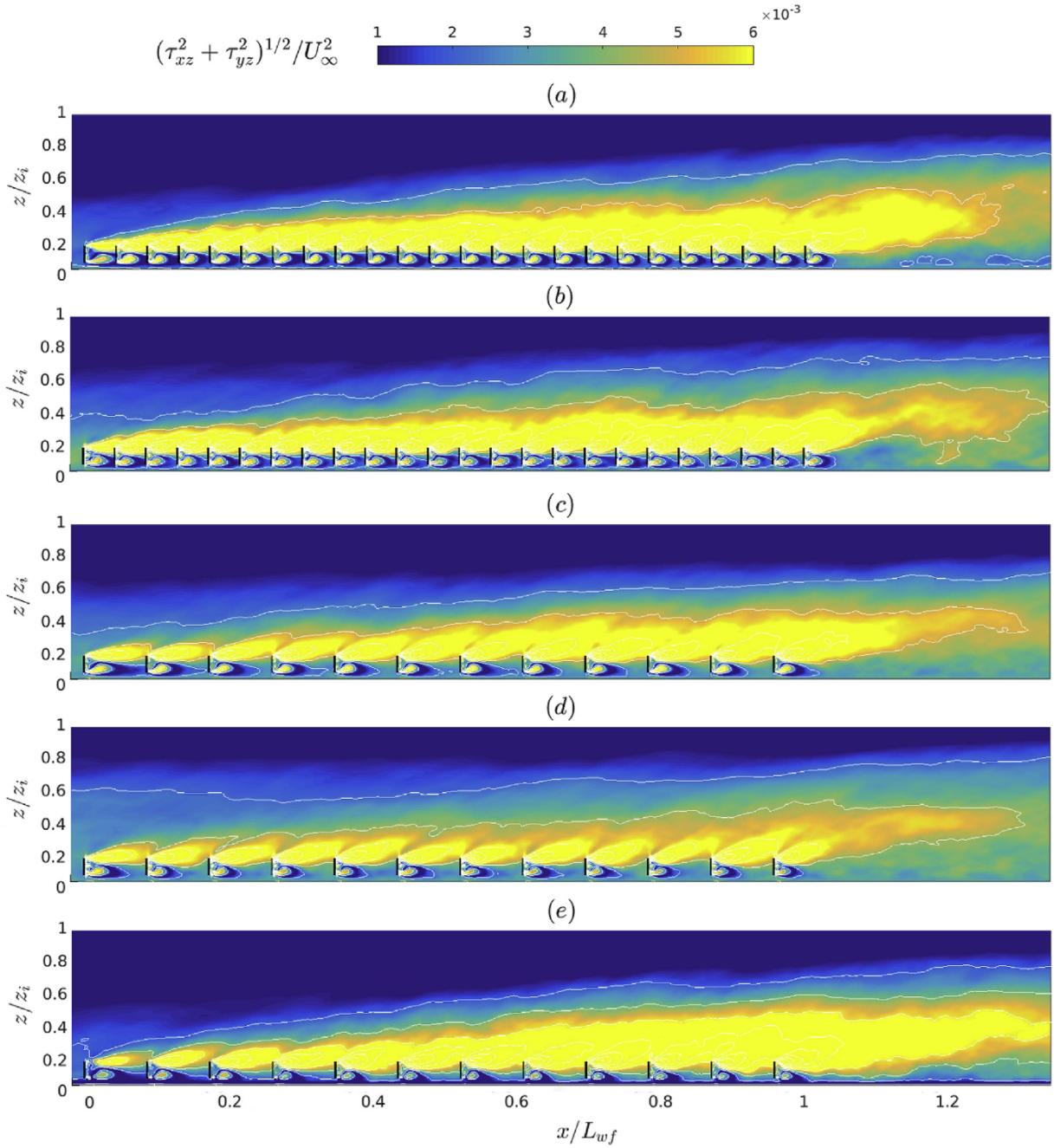

Fig. 3. Time averaged shear stress normalized by the square of the unperturbed inflow wind at the turbines hub-height for the different study cases, (a) AL-1, (b) AL-2, (c) AL-3, (d) AL-4, and (e) ST case. The x-axis is normalized by the streamwise wind farm length, L_{wf} 18*km*, and the y-axis is normalized by the boundary layer height, $z_i = 1000$ m. The black lines denote the location of the wind turbine rotor disk, and the white lines depict iso-countours of shear stress. Note that the figure represents only 25% of the full numerical domain.

interaction with the subjacent ABL flow. The wakes of the turbines in the first rows (row 1 to 9) do not interact laterally with each other. This creates high momentum channels of the size of the inter-rotor space. Alternatively, from row 10 to 14, there exist a transition region, characterized by stronger lateral wake expansion, which narrows the width of the high momentum channels. Approximately at 60% downstream the wind farm the wakes merge in the streamwise direction. For the ST case (see Fig. 2e), due to the unique nature of the wind farm layout, there are no inter-column high momentum channels. In this case, the fully waked regime is reached earlier, approximately at $x = 0.4L_{wf}$. When the spanwise spacing between turbines is doubled (case AL-2 and AL-4), the high momentum channels remain for the entire wind farm length. The only difference between cases AL-2 and AL-4 being the wake-turbine interaction. While in case AL-4 wakes seem to fully recover 85% of the inflow velocity, in case AL-2 there is a constant wake-turbine interaction, with stronger velocity deficits downstream of the wind turbine's rotor disk. In this last case, it is easy to identify a large velocity deficit that encompasses each column of wind turbines. Finally, as a result of the larger streamwise spacing,

Please cite this article as: G. Cortina et al., Mean kinetic energy distribution in finite-size wind farms: A function of turbines' arrangement, Renewable Energy, https://doi.org/10.1016/j.renene.2019.10.148

in case AL-3 the wakes velocity deficit reaches 85%, similar to AL-4 case. However, due to the spanwise proximity between turbines, the high momentum channels seem to persist up to 60% of the wind farm length (up to row 8), where the lateral wake interaction seems to take place, with a much diminished effect compared to the one illustrated in the AL-1 or ST cases. In the later MKE analysis this description will become of use given that the MKE recovery is strongly affected by the channeling effect (*i.e.* the existence or not of the high momentum streaks) and by the lateral turbine's wake interaction.

The vertical shear stress illustrated in Fig. 3 depicts similar features, but at the same time it offers some interesting differences among study cases. First, the largest common feature among study cases is the large values of vertical shear stress at the top of the rotor disk. This footprint extends up to a height of 6D by $x = 1L_{wf}$. Also, note that the intensity of the shear stress depends on the wind farm layout, being the ST case (Fig. 3e) the one illustrating the most intense values and more persistent in terms of downstream extent (showing its presence after $x = 1.3L_{wf}$). Another similar pattern among cases, is weak shear stress at the bottom of the rotor disk, again being the ST case the one illustrating the smallest values and the AL-4 illustrating the larger ones. These phenomena had already been observed in earlier computational studies of infinite size wind farms [33]. Cases AL-1 and AL-2 illustrate a very similar distribution of the vertical sheer stress, with a unique intense and uniform structure at the top of the rotor disk that lasts a little more than $x/L_{wf} = 1.2$. On the contrary, AL-4 case, because of the large inter-turbine streamwise spacing, the shear structures show to be independent for each rotor disk.

4. The mean kinetic energy budget analysis

In this section the distribution of MKE in a finite size wind farm, and its dependence with turbines' spacing is studied. This will further be used to analyze the influence of the wind farm layout in the wind turbine's harvested power and wake recovery mechanisms that contribute to the overall wind farm efficiency. For this purpose, a local wind turbine MKE budget using a CV approach is performed for each study case, as a function of the wind farm row, *i.e.* the downstream distance from the leading edge of the wind farm. This approach has already been used in other works for infinite wind farms [25,27], as well as for finite size wind farms [26]. In this regard, the corresponding MKE budget equation is written as follows,

$$\frac{\partial K}{\partial t} = \underbrace{-\overline{U}_j \frac{\partial K}{\partial x_j} - \frac{\overline{U}_i}{\rho}\frac{\partial \overline{P}}{\partial x_i} - \partial\left(\overline{\tau}_{ij}\overline{U}_i\right)}_{\partial x_j + \overline{\tau}_{ij}\frac{\partial \overline{U}_i}{\partial x_j} + \overline{U}_i \overline{f}_i^{\,\mathrm{wt}}}, \tag{1}$$

where K represents the MKE, $K = \frac{1}{2}\overline{U}_i^2 = \frac{1}{2}(\overline{U}^2 + \overline{V}^2 + \overline{W}^2)$, with $\overline{U}$, $\overline{V}$ and $\overline{W}$ being the streamwise, lateral and vertical mean velocities, respectively, with the over-line denoting the time averaging operation, which is equal to 2 h. The mean pressure is given by $\overline{P}$, and $\overline{f}_i^{\,\mathrm{wt}}$ represents the force imparted on the flow by the wind turbines. The sum of the Reynolds and the subgrid-scale (SGS) shear stress is denoted by $\overline{\tau}_{ij}$. Therefore, from left to right the terms of this equation are the storage of MKE ($\partial K/\partial t$), the advection of MKE (A), the work due to the pressure gradient (P), the flux of MKE (φ), the dissipation of MKE (ε), and the harvested power by the wind turbines (P_{wt}). The MKE of the flow is depleted by the turbines' and turbulence dissipation, replenished by the pressure gradient, and transported by the advection and the turbulent flux of MKE. In a steady state regime, the storage term is null, ($\partial K/\partial t = 0$), and hence the equation can be rewritten as:

$$0 = A + P + \varphi + \varepsilon + P_{wt}, \tag{2}$$

where each term is defined as follows,

$$\underbrace{A = -\overline{U}_j\frac{\partial K}{\partial x_j},\ P = -\frac{\overline{U}_i}{\rho}\frac{\partial \overline{P}}{\partial x_i},\ \varphi = -\partial\left(\overline{\tau}_{ij}\overline{U}_i\right)}_{\partial x_j},$$

$$\varepsilon = \overline{\tau}_{ij}\frac{\partial \overline{U}_i}{\partial x_j},\ P_{wt} = \overline{U}_i\overline{f}_i^{\,\mathrm{wt}}, \tag{3}$$

with $\overline{\tau}_{ij} = \overline{u'_i u'_j} + \overline{\tau}_{ij}^{SGS}$ being the sum of the Reynolds and the subgrid-scale shear stress.

5. Results

5.1. Integrated MKE budget terms

The local CV approach used to study the flow helps to isolate the MKE distribution around the wind turbines and at the same time, disregard the effect of the high momentum channels, but not its contribution to the turbine's wake recovery. Specifically, the MKE terms are first integrated around each turbine, and later averaged for each row of turbines, similar to the analysis of Cortina and Calaf [34]. For the sake of simplicity, results are presented in Fig. 4a for case AL-1, and in Fig. 4b for case AL-4. In these figures, each marker denotes the MKE integrated term for a different wind farm row. For this reason in case AL-1 there are a total of 24 markers, and in case AL-4 a total of 12 markers. The CV that surrounds each wind turbine has dimensions equal to $(L_x^{CV}, L_y^{CV}, L_z^{CV}) = (8D, 3D, 7D/4)$. These dimensions are selected to minimize the MKE budget residual term. Precisely, the box extends between a distance of $2D$-upstream and $6D$-downstream of the disk in the streamwise direction, and $1.5D$ left and right of the hub of the rotor in the cross-streamwise direction, respectively. In the vertical direction, the CV is selected to extend a vertical distance between $z_h - 3D/4$ and $z_h + D$, where z_h is the wind turbine hub-height, equal to 100 m. Additionally, to be able to compare statistics, the CV has equal size for all study cases. Another condition that has been accounted for when determining the streamwise distance of the CV, is to capture the maximum wake region without including the effect of the following wind turbine. Note that having control volumes of equal size to study all cases allows for a one-to-one comparison between cases, being able to understand how differences in the surrounding flow lead to changes within the wind turbines region. Further, in this study the error induced in the corresponding local MKE budgets by considering a fixed control volume size for each study case is being minimized by an optimized control volume size that minimizes the residual for all cases.

By comparing the results from Fig. 4a and b, it can be observed that the MKE deficit due to the wind turbines' power extraction is larger in case AL-4 due to the larger streamwise inter-turbine spacing. Also, it is important to notice how in both scenarios, the first turbine extracts more power than the following ones. The other negative contribution to the MKE budget is the dissipation term, which remains fairly constant along the wind farm length. The pressure term, which acts as a source of MKE, experiences larger values during the four first rows, and then remains constant.

Please cite this article as: G. Cortina et al., Mean kinetic energy distribution in finite-size wind farms: A function of turbines' arrangement, Renewable Energy, https://doi.org/10.1016/j.renene.2019.10.148

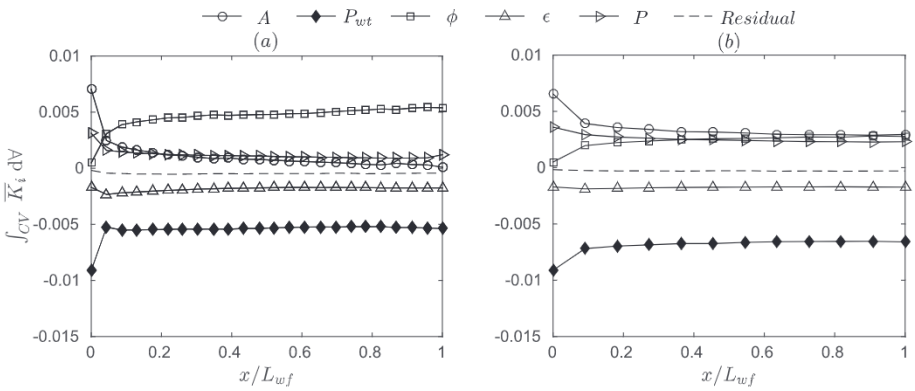

Fig. 4. Control volume integrated MKE terms for the (a) AL-1 case and (b) AL-4 case as a function of the normalized wind farm length, x/L_{wf}. In addition to the MKE terms, the residual is illustrated with a dashed line. The x-axis represents the normalized wind farm length, x/L_{wf}. The y-axis represents the CV integration of the MKE budget terms. The MKE terms are normalized by the wind turbine diameter and the cube of the unperturbed inflow wind at hub-height. Also, the integrated data is normalized by the distances of the CV, $(L_x^{CV} \times L_y^{CV} \times L_z^{CV})$. The CV extends between a distance of 2*D*-upstream and 6*D*-downstream of the wind turbine rotor disk in the streamwise direction, and 1.5*D* left and right of the hub of the rotor in the cross-streamwise direction, respectively. In the vertical direction, the CV is selected to extend a vertical distance between $z_h - 3D/4$ and $z_h + D$, where z_h is the wind turbine hub-height, equal to 100 m.

The most interesting behaviour, is the one illustrated by the MKE transport terms (advection and flux). In the first row of case AL-1, the advection dominates the wake recovery. In the second row of turbines, the advection and flux of MKE show very similar values, and after the second row the advection keeps slightly decreasing up to the end of the wind farm. On the other hand, the flux of MKE has an opposite trend, starting with practically null values, and then progressively increasing as a function of the wind farm length. The same phenomena is illustrated for case AL-4. However, the advection of MKE remains larger than the MKE flux up until row 9, when the flux equals the advection, $\varphi = A$. From this figure it is also interesting to notice that independently of the wind farm layout, the power harvested by the wind turbines is compensated by the sum of advection and flux of MKE, $P_{wt} \approx A + \varphi$. This finding is used in Section 6 to develop the new power predictor model.

From Fig. 4, it can be concluded that the power depleted by the turbines is compensated by MKE transport mechanisms, either through advection or flux of MKE. While advection dominates the MKE recovery at the leading edge of the wind farm, the flux of MKE dominates far from the wind farm leading edge, where there exists a fully developed regime. The contribution by the flux of MKE was also previously observed by other works. For example Meyers and Meneveau [35] and Calaf et al. [33] discussed this same phenomena for horizontally periodic LES wind farm layouts. These works found that the vertical contribution of flux of MKE determined the average turbine power output in the wind farms fully developed

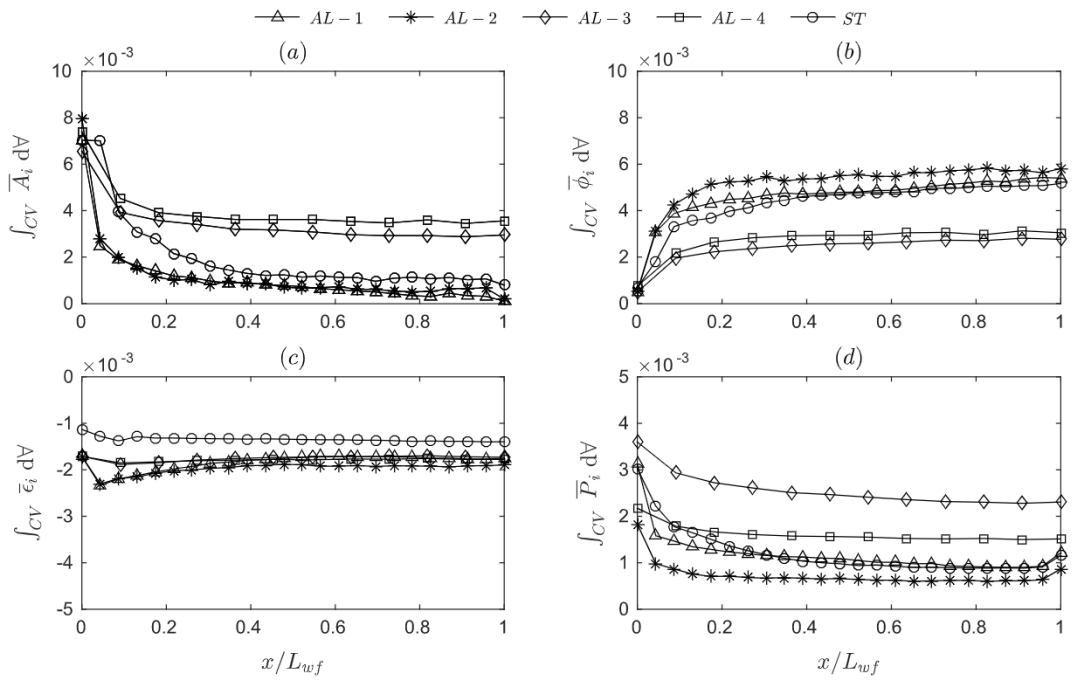

Fig. 5. Control volume integrated MKE terms for the different study cases as a function of the wind farm length for the (a) advection term, (b) flux of MKE, (c) dissipation of MKE and (d) pressure redistribution term. The x-axis represents the normalized wind farm length, x/L_{wf}. The y-axis represents the CV integration of the MKE budget terms. The MKE terms are normalized by the wind turbine diameter and the cube of the unperturbed inflow wind at hub-height. Also, the integrated data is normalized by the distances of the CV, $(L_x^{CV} \times L_y^{CV} \times L_z^{CV})$.

Please cite this article as: G. Cortina et al., Mean kinetic energy distribution in finite-size wind farms: A function of turbines' arrangement, Renewable Energy, https://doi.org/10.1016/j.renene.2019.10.148

regime. Another recent LES study of Stevens et al. [16], also demonstrates that the power output is well correlated with the vertical contribution of kinetic energy flux.

Therefore, it concludes from this analysis that depending on the wind farm layout the contribution of each term can vary, *i.e.* the capacity of the flow to recover by means of advection and/or vertical fluxes depends on the wind farm layout. Further, once the flux of MKE begins to dominate, the flow physics become very similar to those encountered in studies of fully developed wind turbine array boundary layer flows [25].

This is further investigated in Fig. 5, where all terms are individually represented for each study case, allowing proper intercomparison. Because the dissipation and pressure terms (see Fig. 5c and d, respectively) illustrate a weak dependence on the wake recovery, the following discussion will be focused solely on the advection and flux terms.

5.2. Comparison among study cases for the integrated MKE budget terms

As previously anticipated, Fig. 5a demonstrates that for the first rows of turbines the advection dominates the MKE recovery, with its maximum contribution in the 1^{st} row. Then, as the distance from the wind farm leading edge is increased, advection gradually diminishes its contribution, up to a certain distance where it stagnates. The form in which transitions occur between maximum contributions to the corresponding stagnation values is the major difference between study cases. Interestingly, this transition correlates well with the layout of the wind farm. For example, cases AL-1 and AL-2, which have the same s_x inter-turbine spacing, illustrate practically the same trend. Both cases show the smallest advection values after the 1^{st} row. In contrast, cases with a spacing of $2s_x$ (AL-3 and AL-4) illustrate the largest advection values, with the ST case being in between. Moreover, it is interesting to note that while in cases AL-3 and AL-4 the advection term stagnates at $x \approx 0.2L_{wf}$, for cases AL-1, AL-2 and ST it stagnates around $x = 0.4L_{wf}$. An opposite behaviour is observed in the evolution of the flux of MKE (see Fig. 5b). All cases illustrate that the flux is practically negligible for the 1^{st} row of turbines and its contribution progressively increases with the distance from the wind farm leading edge. The larger MKE flux values are observed for the AL-1 and AL-2 cases, and the minimum values are shown by cases AL-3 and AL-4. Note that, the increase of the MKE flux seems to stagnate at the same location as the advection term. This relates with the structure of the wind turbine array boundary layer (WTABL) as describes in Sharma et al. [24].

Furthermore, by comparing Fig. 5a and d, for AL-1, AL-2 and ST cases, a slight increase in the pressure redistribution term at the last row of wind turbines (see Fig. 5d) with a simultaneous slight decrease in advection (see Fig. 5a) can be observed. We hypothesize that the simultaneous pressure recovery and decrease in advection at the further edge of the wind farm in these cases is explained by a transfer of energy from the momentum to the pressure field, in an aim to speed up the wind farm wake recovery process, similarly to what is explained by the actuator disk theory in the flow around a single wind turbine [36].

Finally, there is an interesting phenomena that can be observed in Fig. 5a by comparing AL-1 and ST cases. Both cases have the same geometric mean turbine spacing, and similar behaviours for the flux and pressure redistribution terms. However, the behaviour for the advection term differs, with results showing poor advection values in the AL-1 case compared to the ST case for the first half of the wind farm. After this point, similar results are obtained. This phenomena is again a result of the wind farm layout. By staggering the wind farm the transport of MKE by advection is more prominent, since local acceleration is created between rows of wind turbines which enhances the lateral momentum transport, resulting in larger advection values. Also it should be mentioned that the ST is the case illustrating the smallest dissipation (in absolute value) compared to the rest of the cases (see Fig. 5c).

5.3. Wind farm power output and turbine's efficiency

With the aim to better understand the relationship between the evolution of advection and vertical flux of MKE with the harvested power, Fig. 6a shows the normalized harvested power with respect to the wind farm length, P_i/P_1; i indicating the wind farm's row number.

From Fig. 6a, it can be observed that the power output for the different cases remains approximately constant at locations greater than $0.4L_{wf}$ for cases AL-3, AL-4 and ST. Instead, for cases AL-1 and AL-2 the power stagnates at $0.2L_{wf}$, with downstream power variations of less than 5%. These results are directly related to the evolution of the advection and flux of MKE as previously illustrated in Fig. 5. Additionally, there exist two other phenomena that are worth mentioning. The first one is that for the ST case the normalized power for the second row of turbines is slightly larger than for the first row. This happens because the flow is being deflected laterally by the first row of turbines, creating a local acceleration of the mean wind between the turbines in the first row, see Fig. 2e for more details. The second one is with respect cases AL-1 and AL-2, where the second row of turbines produces less power than the 3rd row. This phenomena is attributed to a reduction of the mean wind velocity due to the interaction with the first row of turbines, combined with a poor influence of the MKE transport mechanisms to recover the velocity deficit.

To complete this analysis, Fig. 6b illustrates the wind farm efficiency (η_{wf}) for each study case, computed as:

$$\eta_{wf} = \frac{1}{NP_1}\sum_{i=1}^{N} P_i, \tag{4}$$

where N is the total number of rows, P_i is the averaged power of each row of turbines, and P_1 is the averaged power of the first row of turbines. The wind farm efficiency is represented in the left y-axis, and it can be seen that case AL-4 ($2s_x \times 2s_y$) is the most efficient wind farm layout of the ones considered, with a 78% efficiency per wind turbine. This is followed by case AL-3 ($2s_x \times s_y$) with a 76%, then case ST (staggered combination with spacing of $s_x \times s_y$) with a 68%, and finally, cases AL-2 ($s_x \times 2s_y$) and AL-1 ($s_x \times s_y$) with an efficiency of 62% and 60%, respectively. These results are in agreement with previous computational works of finite size wind farms [16,24]. Further, by comparing cases AL-1 and AL-2, it is clear that the power output for an aligned configuration shows weak dependence on the spanwise spacing. Contrary by comparing cases AL-1 with AL-3 or AL-4, it is clear that the power output for an aligned configuration shows a strong dependence on the streamwise turbine spacing. Finally, for the staggered configuration the power output depends primarily on the geometric mean of the spanwise and streamwise turbine spacings. In a further step in this analysis, it is very interesting to note the good correlation that exists between the wind farm efficiency and the ratio between the advection and flux of MKE ($TR = A/\varphi$; defining a Transport Ratio). The cases in which advective transport of MKE dominates versus vertical flux transport have a larger wind farm efficiency. This means that one could for example use the TR parameter as a new optimization variable.

Please cite this article as: G. Cortina et al., Mean kinetic energy distribution in finite-size wind farms: A function of turbines' arrangement, Renewable Energy, https://doi.org/10.1016/j.renene.2019.10.148

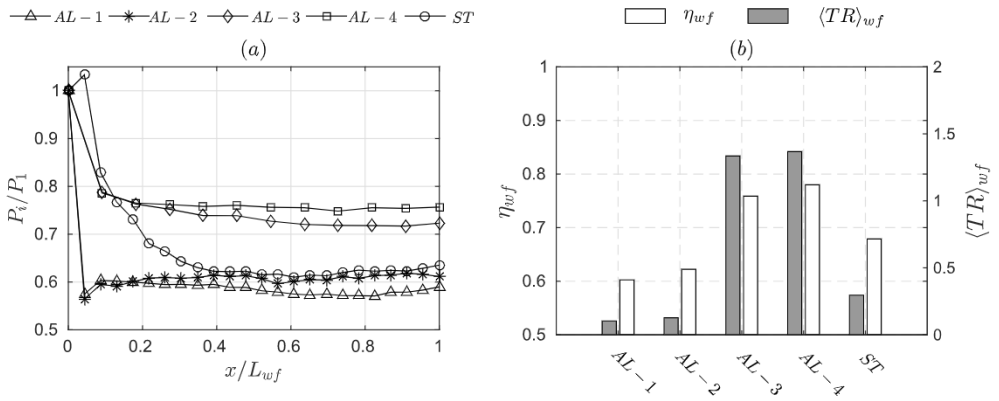

Fig. 6. Representation of the (a) normalized harvested power, P_i/P_1, as a function of the normalized wind farm length; (b) wind farm efficiency, η_{wf}, and transport ratio, *TR*, for the different study cases.

6. Power output predictor model

Based on the analysis of the MKE budget presented in the previous section the wind farms' harvested power is clearly mainly recovered through a combination of advection and flux of MKE,

$$P_i \approx A_i + \varphi_i, \tag{5}$$

where P_i is the average wind turbine harvested power, A_i is the advection and φ_i is the flux of MKE for any given wind farm row, *i*. In fact, assuming Eq. (5) the largest error observed is equal to 15% for the AL-2 case, with an overall average error among the different study cases of only 10%. Further, since the power depleted by the wind turbines at the first row is approximately equal to the advection term, $P_i \approx A_i$, for $i = 1$, and for the furthest downstream row the harvested power is approximately equal to the sum of both transport mechanisms, $P_N \approx A_N + \varphi_N$, one can envision the power at row '*i*' to be approximated by an expression of the type

$$P_i \approx \lambda_i A_1 + (1-\lambda_i)(A_N + \varphi_N). \tag{6}$$

This represents a balance between both extreme cases, with the parameter λ_i being a '*weighting coefficient*' that redistributes the corresponding weight. Because in practice, the integral of the MKE budget terms within a CV surrounding a wind turbine is not a readily available value, an additional approximation can be performed assuming $A_1 \approx P_1$ and $A_N + \varphi_N \approx P_N$, such that

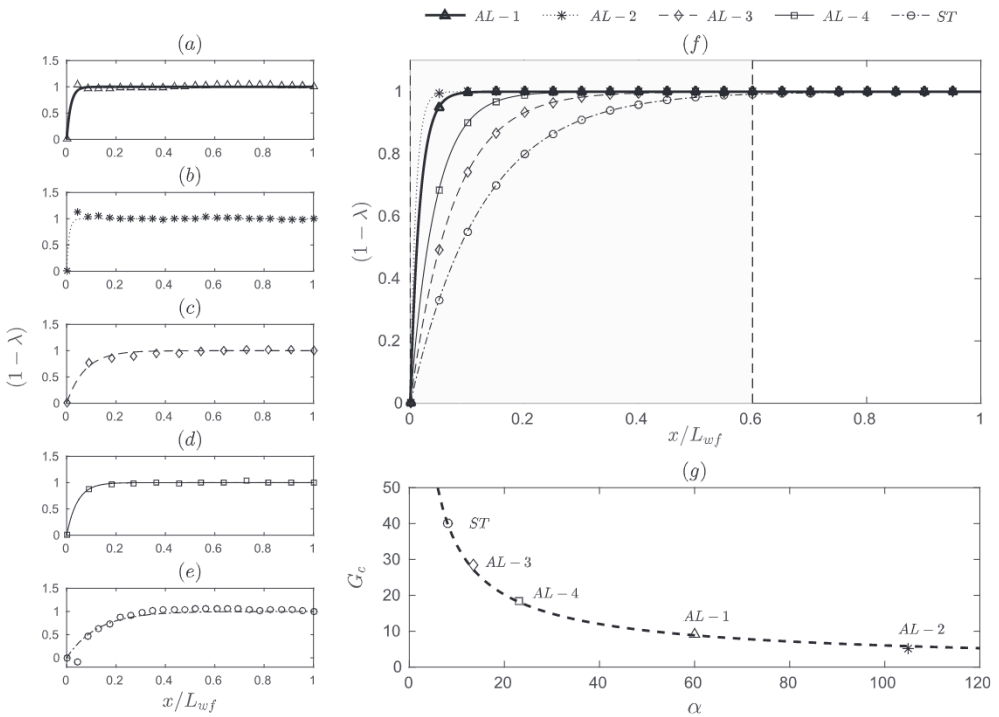

Fig. 7. Representation of the parameter $(1-\lambda)$ for the different study cases. In sub-figures (a) to (e) the markers represent the LES data, and the lines represent the low-order model, for cases AL-1 (a), AL-2 (b), AL-3 (c), AL-4 (d), and ST (e). Sub-figure (f) represents the parameter $(1-\lambda)$ calculated from Eq. (9) for the different study cases. Sub-figure (g) represents the wind farm geometric characteristic parameter, G_c as a function of the wind farm layout correction exponent, α. The dashed line from sub-figure (g) is a fitting of the data, on the form: $G_c = 191\ \alpha^{-3/4}$, or otherwise, $\alpha = 1100\ G_c^{-4/3}$.

Please cite this article as: G. Cortina et al., Mean kinetic energy distribution in finite-size wind farms: A function of turbines' arrangement, Renewable Energy, https://doi.org/10.1016/j.renene.2019.10.148

$$P_i \approx \lambda_i P_1 + (1-\lambda_i)P_N. \tag{7}$$

Additionally, from the results presented earlier, it is further evident that parameter λ_i should be a function of the wind farm layout, and it hence should also change as a function of the wind farm downstream distance. Upon rearrangement of Equation (7), one can get an expression for the weighting coefficient

$$\lambda_i = \frac{P_i - P_N}{P_1 - P_N}, \tag{8}$$

which can then be computed from the LES study cases. This is illustrated in Fig. 7 for the different cases, where the markers in Fig. 7a to e represent the weighting coefficient computed from the LES data-sets, and the lines represent a fitting of the form

$$\lambda_i = \exp\left(-\alpha \frac{x_i}{L_{wf}}\right), \tag{9}$$

where α is a *'layout correction exponent'* dependent on the wind farm layout, x_i is the downstream distance and L_{wf} the total length of the wind farm. From Fig. 7a to e it can be observed that the weighting parameter calculated from Eq. (9) approximates well to the weighting parameter calculated from the LES data. The maximum deviations are observed for the wind turbines located at the second row of the AL-2 and ST cases (see Fig. 7b and e, respectively). Fig. 7f includes all the exponential fittings for the different study cases for easiness of comparison. Interestingly, cases AL-1 and AL-2 practically overlap. These are the cases showing the strongest curvature, and consequently, with the largest layout correction exponent. Besides, the ST case demonstrates to have the most progressive curvature, which expands from the leading edge of the wind farm to $x = 0.6L_{wf}$. Cases AL-3 and AL-4 lay in between the previous mentioned cases, with case AL-4 illustrating a larger layout correction exponent than case AL-3. In Fig. 7f the vertical dashed line indicates that for all study cases, the efficiency of the ABL flow to recover the wake of the wind turbines stagnates. This takes place at $x = 0.6L_{wf}$. At this point, the harvested power remains constant, and the main statistics remain unchanged. Yet, for cases AL-3 and AL-4, this point takes place much earlier, at $x \approx 0.35L_{wf}$ and $x \approx 0.25L_{wf}$; and for AL-1 and AL-2 cases it takes place at $x < 0.1L_{wf}$.

Because the purpose of the layout correction exponent is to specify how the harvested power is redistributed as a function of the wind farm length, and results from previous sections indicate a strong dependence of this with the farm layout, next we develop a non-dimensional relationship between the wind farm arrangement and the layout correction exponent. The non-dimensional parameter is represented by G_c (hereon G_c referenced as the geometric characteristic parameter),

$$G_c = \left(\frac{s_x^2}{s_y s_d}\right)\left(\frac{1}{D\sqrt{\rho_{wf}}}\right), \tag{10}$$

where s_d is the diagonal spacing between turbines, computed as $s_d = \sqrt{(s_x^2 + s_y^2)}$. The wind farm density is represented by ρ_{wf} (*i.e.* wind turbines per unit surface), and D is the turbine's rotor diameter. For staggered cases, s_x should be replaced by s_x' in Eq. (10). In the specific staggered case of this paper $s_x' = 2s_x$, and s_d should be computed as $s_d = \sqrt{(s_x^2 + s_y'^2)}$, where $s_y' = s_y/2$; (see Fig. 8 for more details).

The first factor in Eq. (10) represents the spacings ratio, which accounts for the high momentum streaks, the lateral expansion of the wakes, and direct turbine-wake interaction. The second factor accounts for the clustering effect (*i.e.* the effect of placing more or less turbines per unit surface). As illustrated in Fig. 7g the G_c parameter shows to have an exponential dependence with the layout correction exponent, α. Thus, large values of G_c indicate good wake recovery rates, on the contrary, smaller G_c values indicate poor wake recovery efficiencies. For example, as the streamwise spacing is increased, independently of the spanwise spacing, the density of the wind farm will reduce causing an increase of G_c, meaning more efficient wake recoveries. On the other hand, if the streamwise spacing is decreased and the number of wind turbines is kept constant, G_c would decrease, meaning that the recovery of the wakes will be less efficient. Therefore, the geometric characteristic parameter, G_c, is a non-dimensional parameter that indicates the wake recovery efficiency as a function of the wind farm layout. Notice that, in light of the previous results, we developed the G_c parameter in a way that is highly sensitive to changes on the streamwise spacing and to the wind farm clustering effect, with small sensitivity to changes on the spanwise spacing. From Fig. 7g, it can be observed that the ST case is the one illustrating the largest G_c, and cases AL-1 and AL-2 the smallest values, with cases AL-3 and AL-4 remaining in between (see Table A.1 for more details).

Therefore, if one wants to use the proposed model, one would first determine G_c from the proposed wind farm layout. Next, using the fitting reported in Fig. 7g one would approximate the α coefficient, which would provide a means for afterwards computing λ_i for each turbine row. Realize that this parameter will already provide a measure of each turbine's efficiency. Finally, to compute the

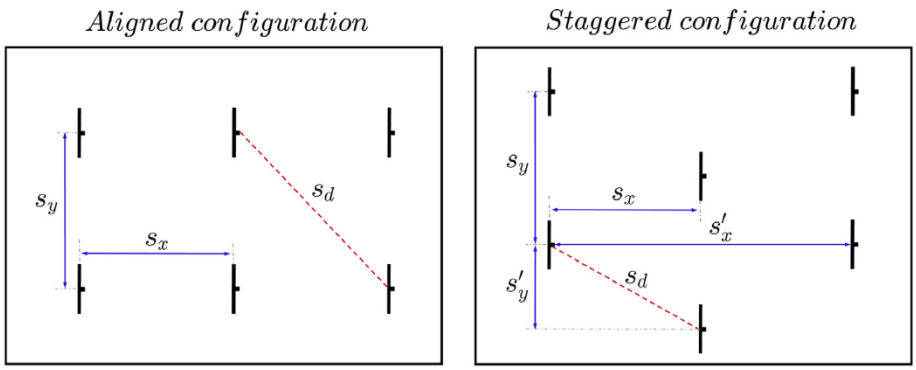

Fig. 8. Inter-turbine spacings for an aligned (left), and a staggered (right) wind farm layout used to compute the *'wind farm geometric characteristic parameter'* depending on the wind farm layout.

Please cite this article as: G. Cortina et al., Mean kinetic energy distribution in finite-size wind farms: A function of turbines' arrangement, Renewable Energy, https://doi.org/10.1016/j.renene.2019.10.148

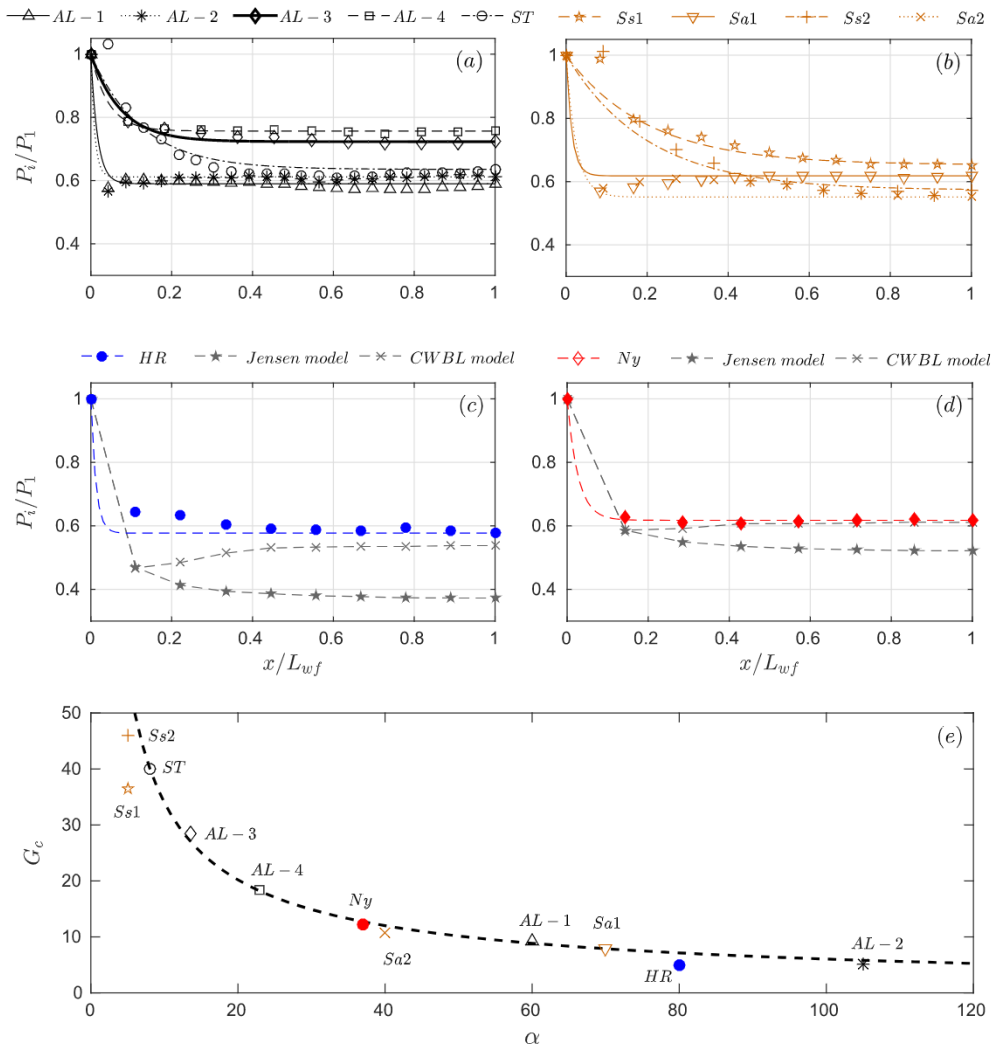

Fig. 9. Sub-figures (a)–(d) illustrate the normalized power as a function of the wind farm length for the different studies used for comparison: (a) LES results from this work, (b) LES data-sets from Stevens et al. [15], and (c) and (d) experimental data from the Horns Rev and Nysted wind farms [8,28,29], respectively. Results illustrated in sub-figures (c) and (d) also depict data-sets from other power predictor models (Jensen model and the CWBL model) from Stevens et al. [21]. Lines represent the power predicted by the low-order model, and the markers represent the LES or experimental measurements. Sub-figure (e) depicts the relationship between the G_c and α for the different cases used to compare the low-order model.

corresponding P_i, one will need P_1, which can be easily approximated as the power of an unperturbed turbine using C_p and the cube of the mean velocity. Finally, P_N can be approximated using additional approximated analytical solutions, such as those for an equivalent surface roughness ($z_{0,eff}$) as in Calaf et al. [33], Yang et al. [14], Meneveau [37], Frandsen et al. [38], from which the power

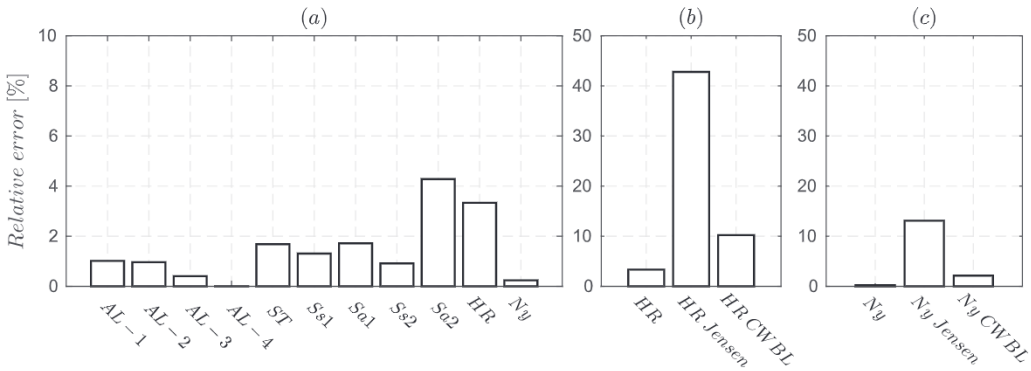

Fig. 10. Sub-figure (a) represents the averaged relative error of the low-order model with respect to the LES data or experimental measurements. Sub-figures (b) and (c) compare the different models data with the experimental measurements for the Horns Rev wind farm (b), and for the Nysted wind farm (c).

Please cite this article as: G. Cortina et al., Mean kinetic energy distribution in finite-size wind farms: A function of turbines' arrangement, Renewable Energy, https://doi.org/10.1016/j.renene.2019.10.148

could then be obtained computing the corresponding modified mean wind.

In the next section 7 this new simplified model is compared with other LES data-sets, and experimental works, completely independent from the numerical data here used for the development of the model.

7. Validation of the low-order model

In order to validate the power predictor model here developed, we compare the results obtained from the low-order model with LES data-sets from Stevens et al. [15], and with experimental data from the Horns Rev and Nysted wind farms [8,28,29]. Also, we compare the results with data-sets from other models [21]. In this regard, Fig. 9a to d shows the normalized harvested power as a function of the wind farm length for the different comparison studies, and Fig. 9e depicts the relationship between the G_c and α parameters. In Fig. 9a to d, lines represent the power predicted by the model, and the markers represent the LES or experimental measurements. The parameters required for the model are further illustrated in Table A.1 from Appendix A for each of the study cases. Also, the averaged relative error, ε_r, between the model and the data is illustrated in Fig. 10, which is computed as:

$$\varepsilon_r[\%] = \frac{100}{N}\sum_{i=1}^{N}\frac{\left|P_i^m - P_i^d\right|}{P_i^d}, \tag{11}$$

where P_i^m is the power predicted by the model for each row of turbines, and P_i^d is the power obtained from the different data-sets. The total number of turbine rows is represented by N.

First in Fig. 9a the power estimated by the model is compared to the LES data-set from this work. It can be observed that the model accurately predicts the power for cases AL-3 and AL-4. However, it is not capable to capture the second row of the ST, AL-1 and AL-2 cases. For example, for the second row of the ST case, the model under-predicts the harvested power, while for the AL-1 and AL-2 cases, the model over-predicts the power. Overall, the model shows a good performance, with average relative errors smaller than 2%, (see Fig. 10a).

In Fig. 9b the prediction of the model is compared with two aligned and two staggered cases from Stevens et al. [15] work. This comparison analysis illustrates similar results to the ones illustrated in Fig. 9a. For the staggered cases, *Ss1* and *Ss2*, the model is not able to estimate the power of the second row of turbines, but it seems to properly capture the power of further downstream rows. For the aligned cases, specifically for the *Sa1* case, the model seems to over-predict the power from rows 2, 3 and 4; and for the *Sa2* case, the model properly captures the power of the second row, but instead, under-predicts rows from 3 to 7. Overall the average relative error is very small, approximately 4%.

In Fig. 9c and d, the model is compared with experimental measurements from the Horns Rev and Nysted wind farms [8,28,29], respectively. Also, in these cases the model is further compared with two other models, the Jensen model and the coupled wake boundary layer (CWBL) model (see Stevens et al. [21] for more details about the results and applicability of both models). Regarding the field measurements, the average wind speed of both selected cases is 8 ± 0.5 ms^{-1}, for wind directions of 270° for the Horns Rev wind farm, and 178° for the Nysted wind farm. Results from Fig. 9c demonstrate that the model slightly under-predicts the power for rows 2 to 4 for the Horns Rev wind farm. This corresponds to a relative error of approximately 3%. It is relevant to note that the data from the Jensen and CWBL models present much larger errors, and under-predictions for all rows except of the first one. The error illustrated for the Jensen model is of the order of 40%, and the CWBL model shows a better performance with an overall 10% averaged relative error.

Interestingly, in Fig. 9d the model shows an excellent estimation of the Nysted wind farm experimental measurements, with the CWBL model also demonstrating a good agreement. Instead, the Jensen model data is the one illustrating the largest discrepancies, with an average relative error of 12%.

Another interesting feature revealed by the relationship between the G_c and α parameters from Fig. 9e is that there seems to exist three different groups of wind farms. The first group is composed by the staggered configurations, which are characterized by having large G_c and small α values, ($G_c > 30$ and $\alpha < 10$). The second group is composed by aligned configurations with a large streamwise spacing, with $10 < G_c < 30$ and $10 < \alpha < 50$. And the third group is constituted by wind farms with small streamwise spacing, and characterized by small G_c and large α values, ($G_c < 10$ and $\alpha > 50$).

From this section, we can conclude that the new model seems to perform well for all the study cases considered in this work, with averaged errors smaller than 5% (see Fig. 10). Therefore, it is now possible to estimate the effectiveness of recovering the wake of the wind turbine just as a function of the wind farm layout, and consequently to estimate the power output as a function of the wind farm row, with the input of geometrical characteristics of a given wind farm.

8. Summary & conclusions

In this work we explored the effectiveness of the atmospheric flow to recover wind turbine wakes by means of large eddy simulations of finite size wind farms. The kinetic energy redistribution has been studied by evaluating the mean kinetic energy budget as a function of the wind farm length, under neutral conditions for a finite size wind farm.

Results are in agreement with previous works on an infinite long wind farm, where two different kinetic energy transport mechanisms to recover the velocity deficit downstream of the wind turbines exist, advection and flux of MKE. Both mechanisms show a strong dependence on the wind farm layout. Consequently, they drive the effectiveness on recovering the turbine's wakes, and thus, the total energy available for power extraction. It has been shown that for the first rows of turbines, the advection is the transport mechanism that dominates. The physical interpretation of this finding is that, in the first rows of a wind farm the total amount of kinetic energy transported downwind of the rotor disk is mainly transported by the mean wind. On the other hand, for the last rows of turbines the flux of MKE is the transport mechanism that dominates. In other words, the wakes recover by means of kinetic energy transported by turbulence mechanisms. For rows in between, a smooth transition exists between both mechanisms. Furthermore, it has also been demonstrated that the power output for an aligned configuration shows weak dependence on the spanwise spacing, but a strong dependence on the streamwise spacing which agrees with previous findings published in the literature [14,16,39,40]. Additionally, results have also demonstrated that for the staggered wind farm configuration the power output depends primarily on the geometric mean of the spanwise and streamwise turbine spacings, due to the unique nature of the wind farm layout and because of the absence of inter-column high momentum streaks. Also, it has been shown how wind turbines layout strongly

Please cite this article as: G. Cortina et al., Mean kinetic energy distribution in finite-size wind farms: A function of turbines' arrangement, Renewable Energy, https://doi.org/10.1016/j.renene.2019.10.148

influences the overall wind farm efficiency. With large streamwise spacing $s_x \approx 15D$ aligned configurations showing the largest efficiencies per wind turbine unit, and aligned configurations with small streamwise spacings, $s_x \approx 7.5D$, presenting the weakest efficiencies. With staggered configurations laying in between.

Finally, a new low-order power predictor model has been introduced that estimates the efficiency of the wind turbines as a function of their location within the wind farm, and only requiring as an input the wind farm geometrical characteristics. The low-order model has been validated with other LES data and field measurements. Such comparison under-covered a good performance of the model, with average relative errors smaller than 5%.

As a natural follow up of this work, it would be interesting to study the effect of having a lateral finite size wind farm. Enabling the side flow circulation around the wind farm we believe will have an effect on the wake recovery process, given the potential reduction in flow blockage induced by the farm. At the same time there will most probably exist a change in the development of the wind turbine array boundary layer. Moreover, a next step would be to extend this analysis under the influence of atmospheric stratification [41] and determine whether the model is valid under such conditions. We hypothesize that the *'geometrical characteristic'* parameter would have to be modified in order to include the effects of ABL stratification. A proper stability correction parameter would account for the fact that under unstable ABL conditions the wake recovery rate will increase, (*i.e.* a more efficient wake recovery would exists). Instead, under stable conditions this same parameter would have to account for weaker wake recovery rates. Also, accounting for the outer-layer effects such as Coriolis forces and the capping inversion, such performed in Allaerts and Meyers [26], would be of great interest.

Acknowledgements

This research has been supported with the start-up funds provided by the Mechanical Engineering Department at University of Utah to Prof. M. Calaf. The authors would like to acknowledge the computational support provided by the Center for High Performance Computing (CHPC) at University of Utah. V.S. would like to acknowledge the support received through the Swiss National Science Foundation (project no. 200021134892/1 and 20020 125092), ETH Domain Centre for Competence in Environmental Sustainability, NSERC Discovery Grant (MBP), Swiss National Supercomputing Center (CSCS), Scientific IT and Application Support (SCITAS) group at EPFL.

Appendix A. Large Eddy Simulation framework

To solve the neutrally stratified atmospheric boundary layer flow, the filtered Navier-Stokes equations (Eq. (A.1)) for an incompressible fluid are integrated in rotational form to assure conservation of energy and mass of the inertial terms [42] together with the continuity equation (Eq. (A.2)),

$$\frac{\partial \tilde{u}_i}{\partial t} + \tilde{u}_j\left(\frac{\partial \tilde{u}_i}{\partial x_j} - \frac{\partial \tilde{u}_j}{\partial x_i}\right) = -\frac{1}{\rho}\frac{\partial p^*}{\partial x_i} - \frac{\partial \tilde{\tau}_{ij}}{\partial x_j} + f_i{}^{\mathrm{wt}}, \tag{A.1}$$

$$\frac{\partial \tilde{u}_i}{\partial x_i} = 0, \tag{A.2}$$

The flow is forced using a constant pressure gradient, such that $\frac{1}{\rho}\frac{\partial p_\infty}{\partial x} = 1$, with all variables being normalized with the surface friction velocity, u_*, and the height of the boundary layer, z_i. In the equations, a tilde ($\tilde{}$) represents the LES filtering operation at the grid-size Δ, with the index notation used to specify rectangular Cartesian coordinates $i = 1, 2, 3 = x, y, z$. The deviatoric part of the filtered shear stress is modeled using the classic Smagorinsky subgrid-scale model [43] with constant smagorinsky coefficient $C_s = 0.16$ together with a damping function to control the Smagorinsky coefficient close to the surface [44]. The modified kinematic pressure term (p^*) includes the filtered pressure term and the trace of the SGS tensor $\left(\tilde{p}/\rho + \tilde{\tau}_{kk}/3 + \frac{1}{2}\tilde{u}_j\tilde{u}_j\right)$. The forcing exercised by the wind turbines on the flow is represented by means of a body force, $f_i{}^{\mathrm{wt}}$. The wind turbine force is represented using the traditional actuator-disk with rotation model (ADR, see Wu and Porté-Agel [32]). It is important to note that as it is traditional in LES of atmospheric flows, the viscous effects are neglected and the flow is therefore characterized by a very large Reynolds number. The equations are integrated using a pseudo-spectral approach in the horizontal direction with a second-order finite differences scheme in the vertical direction, similar to Moeng [45] and Albertson and Parlange [46]. Because of the implicit periodicity introduced when integrating the equations using spectral methods, the simulated flow, in practise has an infinite horizontal span. The equations are dealiazed using the 3/2-rule [47], and time-integrated using a second order Adam-Bashfort scheme. The numerical algorithm is fully parallelized using the Message-Passing Interface (MPI) where the pipeline Thomas algorithm [48] is used to parallelize the pressure solver. The code uses a zero-flux and zero-shear lid with the vertical velocity and the vertical gradients of the horizontal velocity components equal to zero. At the surface, the non-slip condition is imposed for the vertical velocity, and because of the staggered grid, an equivalent shear stress is imposed at the first grid point for the horizontal velocities. The shear stress at the surface is parametrized using an adaptation of Monin-Obukhov similarity theory [49], similar to Refs. [50–52].

$$\tau_{i,3}(x, y, z_1) = -\left[\frac{\kappa\sqrt{(\widehat{\tilde{u}}_1^2 + \widehat{\tilde{u}}_2^2)}}{\ln(z_1/z_0)}\right]^2 n_i. \tag{A.3}$$

Note that z_1 indicates the height of the first grid point where the horizontal velocity components are computed ($\Delta_z/2$) and where the shear stress is applied, and z_0 represents the ground surface roughness, in this study imposed as homogeneous and with a value of $z_0 = 10^{-4} z_i$ (where z_i is the initial inversion height, which will be used as a normalization length-scale). Further, n_i is a unitary directional vector, $n_i = \widehat{\tilde{u}}_i/\sqrt{\widehat{\tilde{u}}_1^2 + \widehat{\tilde{u}}_2^2}$ where 'i' indicates any of the horizontal plane-parallel directions ($i = 1, 2$). In addition to the shear stress at the surface, the vertical derivatives of the horizontal velocities are also parametrized at the first grid point (z_1) using Monin-Obukhov similarity theory [53],

$$\partial_3 \tilde{u}_i(x, y, z_1) = \left(\frac{\sqrt{\tau}}{\kappa z}\right) n_i, \tag{A.4}$$

with $\tau = \sqrt{\tau_{1,3}^2 + \tau_{2,3}^2}$. Because we are interested in modeling the atmospheric flow under neutral conditions, the stability correction functions ($\psi(z/L)$) are set equal to zero. The solver however is capable of solving for unstable and stable conditions as well.

Please cite this article as: G. Cortina et al., Mean kinetic energy distribution in finite-size wind farms: A function of turbines' arrangement, Renewable Energy, https://doi.org/10.1016/j.renene.2019.10.148

Table A.1
Parameters used in the power model to compute the geometric characteristic parameter, G_c. From left to right, case of study, number of turbines, rotor diameter (D), spacing of the wind farm (s_x, s_y), wind farm density (ρ_{wf}) in units of number of turbines per unit area in kilometers squared, and geometric characteristic parameter (G_c).

Study case	No. of turbines	D [m]	Spacing (s_x, s_y)	ρ_{wf} [# of turbines/km^2]	G_c
LES study cases of this work					
AL-1	192	100	7.5D, 3.93D	3.34	9.18
AL-2	96	100	7.5D, 7.86D	1.70	5.06
AL-3	96	100	15D, 3.93D	1.70	28.36
AL-4	48	100	15D, 7.86D	0.85	18.36
ST	192	100	7.5D, 3.93D	3.34	40.11
LES study cases of Stevens et al. [15]					
Ss1	78	100	7.85D, 5.23D	2.43	34.50
Sa1	78	100	7.85D, 5.23D	2.43	8.00
Ss2	72	100	7.85D, 3.49D	3.65	45.97
Sa2	72	100	7.85D, 3.49D	3.65	10.76
Experimental measurements from Horns Rev and Nysted wind farms [8,28,29]					
HR	80	80	7D, 6.95D	3.21	4.98
Ny	72	82.4	10.4D, 5.74D	2.47	12.26

References

[1] P.a. Fleming, P.M.O. Gebraad, S. Lee, J.W. van Wingerden, K. Johnson, M. Churchfield, J. Michalakes, P. Spalart, P. Moriarty, Evaluating techniques for redirecting turbine wakes using SOWFA, Renew. Energy 70 (2014) 211–218. ISSN 09601481.
[2] P.M.O. Gebraad, J.W. van Wingerden, A control-oriented dynamic model for wakes in wind plants, in: Journal of Physics: Conference Series, vol. 524, 2014, 012186. ISSN 1742–6596.
[3] M.J. Churchfield, P. Fleming, B. Bulder, S.M. White, Wind turbine wake-redirection control at the Fishermen's Atlantic city windfarm, in: Offshore Technology Conference, May, Offshore Technology Conference, 2015.
[4] I. Antoniou, H.E. Jørgensen, T. Mikkelsen, S. Frandsen, R. Barthelmie, C. Perstrup, M. Hurtig, Offshore wind profile measurements from remote sensing instruments, in: European Wind Energy Conference, 2006.
[5] A. Peña, C.B. Hasager, S.-E. Gryning, M. Courtney, I. Antoniou, T. Mikkelsen, Offshore wind profiling using light detection and ranging measurements, Wind Energy 12 (2) (2009) 105–124.
[6] Y. Käsler, S. Rahm, R. Simmet, M. Kühn, Wake measurements of a multi-MW wind turbine with coherent long-range pulsed Doppler wind lidar, J. Atmos. Ocean. Technol. 27 (9) (2010) 1529–1532.
[7] G.V. Iungo, Y.-T. Wu, F. Porté-Agel, Field measurements of wind turbine wakes with lidars, J. Atmos. Ocean. Technol. 30 (2) (2013) 274–287.
[8] K.S. Hansen, R.J. Barthelmie, L.E. Jensen, A. Sommer, The impact of turbulence intensity and atmospheric stability on power deficits due to wind turbine wakes at Horns Rev wind farm, Wind Energy 15 (1) (2012) 183–196.
[9] L.P. Chamorro, F. Porté-Agel, Effects of thermal stability and incoming boundary-layer flow characteristics on wind-turbine wakes: a wind-tunnel study, Boundary-Layer Meteorol. 136 (3) (2010) 515–533.
[10] R.B. Cal, J. Lebrón, L. Castillo, H.S. Kang, C. Meneveau, Experimental study of the horizontally averaged flow structure in a model wind-turbine array boundary layer, J. Renew. Sustain. Energy 2 (1) (2010), 013106.
[11] L.P. Chamorro, R. Arndt, F. Sotiropoulos, Turbulent flow properties around a staggered wind farm, Boundary-Layer Meteorol. 141 (3) (2011) 349–367.
[12] G.V. Iungo, Experimental characterization of wind turbine wakes: wind tunnel tests and wind LiDAR measurements, J. Wind Eng. Ind. Aerodyn. 149 (2016) 35–39.
[13] J. Meyers, C. Meneveau, Optimal turbine spacing in fully developed wind farm boundary layers, Wind Energy 15 (2) (2012) 305–317.
[14] X. Yang, S. Kang, F. Sotiropoulos, Computational study and modeling of turbine spacing effects in infinite aligned wind farms, Phys. Fluids 24 (11) (2012) 115107.
[15] R.J. Stevens, D.F. Gayme, C. Meneveau, Large eddy simulation studies of the effects of alignment and wind farm length, J. Renew. Sustain. Energy 6 (2) (2014), 023105.
[16] R.J. Stevens, D.F. Gayme, C. Meneveau, Effects of turbine spacing on the power output of extended wind-farms, Wind Energy 19 (2) (2016) 359–370.
[17] Y.-T. Wu, F. Porté-Agel, Large-eddy simulation of wind-turbine wakes: evaluation of turbine parametrisations, Boundary-Layer Meteorol. 138 (3) (2011) 345–366.
[18] Y.-T. Wu, F. Porté-Agel, Simulation of turbulent flow inside and above wind farms: model validation and layout effects, Boundary-Layer Meteorol. (2013) 1–25.
[19] N. Jensen, A Note on Wind Generator Interaction, Risø-M, 1983, ISBN 87-550-0971-9, pp. 1–16. No.2411.
[20] I. Katic, J. Højstrup, N.O. Jensen, A simple model for cluster efficiency, in: European Wind Energy Association Conference and Exhibition, 1986, pp. 407–410.
[21] R.J. Stevens, D.F. Gayme, C. Meneveau, Generalized coupled wake boundary layer model: applications and comparisons with field and LES data for two wind farms, Wind Energy 19 (11) (2016) 2023–2040.
[22] R.J. Stevens, B.F. Hobbs, A. Ramos, C. Meneveau, Combining economic and fluid dynamic models to determine the optimal spacing in very large wind farms, Wind Energy 20 (3) (2017) 465–477.
[23] V.S. Bokharaie, P. Bauweraerts, J. Meyers, Wind-farm layout optimisation using a hybrid Jensen-LES approach, Wind Energy Science 1 (2) (2016) 311.
[24] V. Sharma, G. Cortina, F. Margairaz, M. Parlange, M. Calaf, Evolution of flow characteristics through finite-sized wind farms and influence of turbine arrangement, Renew. Energy 115 (January 2018) 1196–1208.
[25] G. Cortina, M. Calaf, R.B. Cal, Distribution of mean kinetic energy around an isolated wind turbine and a characteristic wind turbine of a very large wind farm, Physical Review Fluids 1 (7) (2016), 074402.
[26] D. Allaerts, J. Meyers, Boundary-layer development and gravity waves in conventionally neutral wind farms, J. Fluid Mech. 814 (2017) 95–130.
[27] G. Cortina, V. Sharma, M. Calaf, Wind farm density and harvested power in very large wind farms: a low-order model, Physical Review Fluids 2 (7) (2017), 074601.
[28] R. Barthelmie, S. Frandsen, K. Hansen, J. Schepers, K. Rados, W. Schlez, A. Neubert, L. Jensen, S. Neckelmann, Modelling the impact of wakes on power output at Nysted and Horns Rev, in: European Wind Energy Conference, 2009.
[29] R.J. Barthelmie, S.T. Frandsen, O. Rathmann, K.S. Hansen, E. Politis, J. Prospathopoulos, J. Schepers, K. Rados, D. Cabezón, W. Schlez, et al., Flow and Wakes in Large Wind Farms: Final Report for UpWind WP8, Tech. Rep, Danmarks Tekniske Universitet, Risø Nationallaboratoriet for Bæredygtig Energi, 2011.
[30] J. Smagorinsky, General circulation experiments with the primitive equations: I. The basic experiment, Mon. Weather Rev. 91 (3) (1963) 99–164.
[31] J. Meyers, C. Meneveau, Large Eddy Simulations of large wind-turbine arrays in the atmospheric boundary layer, 48th AIAA Aerospace Sciences Meeting Including the New Horizons Forum and Aerospace Exposition .
[32] Y.-T. Wu, F. Porté-Agel, Large-eddy simulation of wind-turbine wakes: evaluation of turbine parametrizations, Boundary-Layer Meteorol. 138 (2011) 345–366.
[33] M. Calaf, C. Meneveau, J. Meyers, Large eddy simulation study of fully developed wind-turbine array boundary layers, Phys. Fluids 22 (2009), 015110.
[34] G. Cortina, M. Calaf, Turbulence upstream of wind turbines: a large-eddy simulation approach to investigate the use of wind lidars, Renew. Energy 105 (2017) 354–365. ISSN 0960–1481.
[35] J. Meyers, C. Meneveau, Large eddy simulations of large wind-turbine arrays in the atmospheric boundary layer, in: 48th AIAA Aerospace Sciences Meeting Including the New Horizons Forum and Aerospace Exposition, American Institute of Aeronautics and Astronautics, 2010.
[36] T. Burton, N. Jenkins, D. Sharpe, E. Bossanyi, Wind Energy Handbook, John Wiley & Sons, 2011.
[37] C. Meneveau, The top-down model of wind farm boundary layers and its applications, J. Turbul. 13 (2012) N7.
[38] S. Frandsen, R. Barthelmie, S. Pryor, O. Rathmann, S. Larsen, J. Højstrup, M. Thøgersen, Analytical modelling of wind speed deficit in large offshore wind farms, Wind Energy: An Int. J. Prog. Appl. Wind Power Convers. Technol. 9 (1–2) (2006) 39–53.
[39] C.L. Archer, S. Mirzaeisefat, S. Lee, Quantifying the sensitivity of wind farm performance to array layout options using large-eddy simulation, Geophys. Res. Lett. 40 (18) (2013) 4963–4970.
[40] N.S. Ghaisas, C.L. Archer, Geometry-based models for studying the effects of wind farm layout, J. Atmos. Ocean. Technol. 33 (3) (2016) 481–501.
[41] N.S. Ghaisas, C.L. Archer, S. Xie, S. Wu, E. Maguire, Evaluation of layout and

Please cite this article as: G. Cortina et al., Mean kinetic energy distribution in finite-size wind farms: A function of turbines' arrangement, Renewable Energy, https://doi.org/10.1016/j.renene.2019.10.148

atmospheric stability effects in wind farms using large-eddy simulation, Wind Energy 20 (7) (2017) 1227–1240.
[42] Y. P, S.A. Orzag, Numerical computation of turbulent shear flows, Adv. Geophys. 1 (224) (1974) 225–236.
[43] J. Smagorinsky, General circulation experiments with the primitive equations, Mon. Weather Rev. 91 (3) (1963) 99–164.
[44] P.J. Mason, D.J. Thomson, Stochastic backscatter in large-eddy simulations of boundary layers, J. Fluid Mech. 242 (1992) 51–78.
[45] C.-h. Moeng, A large-eddy-simulation model for the study of planetary boundary-layer turbulence, J. Atmos. Sci. 41 (13) (1984) 2052–2062.
[46] J.D. Albertson, M.B. Parlange, Natural integration of scalar fluxes from complex terrain, Adv. Water Resour. 23 (3) (1999) 239–252.
[47] Z.T. Canuto C, M. Hussainii, A. Quarteroni, Spectral Methods in Fluid Dynamics, Springer-Verlag, Berlin, 1988.
[48] A. Povitsky, P.J. Morris, A higher-order compact method in space and time based on parallel implementation of the Thomas algorithm, J. Comput. Phys. 161 (1) (2000) 182–203.
[49] A.S. Monin, A.M. Obukhov, Basic laws of turbulent mixing in the surface layer of the atmosphere, English translation by John Miller, Tr. Akad. Nauk SSSR Geofiz. Inst 24 (151) (1959) 163–187, 1954.
[50] M.B. Parlange, W. Brustaert, Regional shear stress of broken forest from radiosonde wind profiles in the unstable surface layer, Boundary-Layer Meteorol. 64 (4) (1993) 355–368.
[51] E. Bou-Zeid, C. Meneveau, M.B. Parlange, A scale-dependent Lagrangian dynamic model for large eddy simulation of complex turbulent flows, Phys. Fluids 17 (2) (2005) 1–18.
[52] M. Hultmark, M. Calaf, M.B. Parlange, A new wall shear stress model for atmospheric boundary layer simulations, J. Atmos. Sci. 70 (11) (2013) 3460–3470.
[53] W. Brutsaert, M.B. Parlange, The unstable surface layer above forest: regional evaporation and heat flux, Water Resour. Res. 28 (12) (1992) 3129–3134.

Please cite this article as: G. Cortina et al., Mean kinetic energy distribution in finite-size wind farms: A function of turbines' arrangement, Renewable Energy, https://doi.org/10.1016/j.renene.2019.10.148